Supplemental Information

Design of the new generation of a device for magnetic ranking cytometry (MagRC)

In the original MagRC device, the long length of the chip leads to long residence times, allowing cells to settle towards the end of the channel. However, its large size significantly reduces the number of chips that can fit on a wafer, and thus the rate of chip fabrication. In order to increase the rate of chip fabrication while maintaining a comparable capture efficiency, we opted to increase the width of the zones steadily, which in turn could reduce the length of device by half (Figure S1). To this end, we assumed that cells with high, medium and low magnetic loadings were captured in three capture regions that are: zones 1-4, zones 5-7 and zones 8-10, respectively. The device design was optimized based on capturing low magnetic loading cells with high efficiency. The widths of the channel in different regions were selected according to two criteria: (1) the low magnetic loading cells should be settled before reaching zone 8, (2) All the low magnetic loading cells should be captured within zone 8, 9 and 10. The settling and capture time can be calculated according to the following equation:

$$t = \frac{L \times W \times h}{Q} \qquad (1)$$

where Q, L, W and h define flow rate, length, width, and height of microfluidic device, respectively.

Similar to MagRC, we used circular nickel micro-magnets patterned within the channel to enhance the externally applied magnetic field. In MagRC, the nickel radii increase from 136 μm to 235 μm by 1 μm intervals. In the next generation of MagRC device, the nickel radii increase by 10 μm from r=145 μm to r=235 μm. As a result, cells are exposed to a larger magnetic force compared to MagRC. Therefore, the settling and capture time of cells in the next generation of MagRC ($t_{s\text{-}10}$ and $t_{c\text{-}10}$) device are less than settling and capture time in the MagRC device ($t_{s\text{-}100}$ and $t_{c\text{-}100}$).

Settling time: $t_{s-100} = \alpha \times t_{s-10}$ (2)

Capture time: $t_{c-100} = \beta \times t_{c-10}$ (3)

We assumed that the flow rate in both devices is equal. Also, the two devices had the same height. It is worth noting that in MagRC, the width is kept constant along the length of the channel (W). According to these considerations, substituting equation (1) into equation (2) and (3) results in:

Settling time: $W \times L_{s-100} = \alpha \times W_{s-10} \times L_{s-10}$ (4)

Capture time: $W \times L_{c-100} = \beta \times W_{c-10} \times L_{c-10}$ (5)

In the next generation of MagRC, low magnetic loading cells should be settled by zone 8 where they have passed capture regions allocated to high and medium magnetic loading cells. We assumed an average width of W_1 and W_2 for zones 1-4 and zone 5-7, respectively, where high and medium magnetic loading cells are become captured. Therefore, we can re-write the equation 4 as:

$$W \times L_{s-100} = \alpha \times (W_1 L_1 + W_2 L_2) \qquad (6)$$

The low magnetic loading cells should be captured in zone 8, 9 and 10. We assumed that the average width of these three zones is W_3 and the length is L_3. Therefore, equation 5 can be written as:

$$W \times L_{c-100} = \beta \times W_3 \times L_3 \qquad (7)$$

Dividing equation 6 by 7 results in:

$$\frac{L_{s-100}}{L_{c-100}} = \frac{\alpha}{\beta} \times \frac{W_1 L_1 + W_2 L_2}{W_3 L_3} \qquad (8)$$

α and β are constants reflecting the effect of nickel micro-magnets on the settling and capture times. These constants are proportional to the distance a cell travels:

$$\frac{\alpha}{\beta} = \frac{L_1 + L_2}{L_3} \qquad (9)$$

Based on equation 9, equation 8 can be written as:

$$\frac{L_{s-100}}{L_{c-100}} = \frac{L_1 + L_2}{L_3} \times \frac{W_1 L_1 + W_2 L_2}{W_3 L_3} \qquad (10)$$

We assumed that all three regions of the device have equal length (equation 11). By substituting L_{s-100} and L_{c-100} from the modeling of MagRC ($L_{s-100} = 53\ mm$ and $L_{c-100} = 28\ mm$), the relation between the widths of the new device in different regions can be written as:

$$L_1 = L_2 = L_3 \qquad (11)$$

$$\frac{W_1 + W_2}{W_3} \sim 1 \qquad (12)$$

Based on this equation, we started the device design by selecting $W_1, W_2,$ and W_3 to be 5, 10 and 15 mm, respectively. These widths represent the average width of zones in different regions where high, medium and low magnetic loading cells are captured.

Capture zone calculation

Similar to the MagRC device, a capture zone is defined as the region where the magnitudes of the magnetic and drag force are comparable, meaning that any cells that pass through a capture zone are expected to get captured. For a cell coated with many magnetic nanoparticles, the capture zone generated by small micro-magnet in regions with high linear velocity is sufficiently large to ensure capture. Therefore, cells with high magnetic loadings are captured in earlier zones which have smaller widths and micro-magnets. However, cells coated with a low number of magnetic nanoparticles are deflected only if they are close enough to the bottom of the chip and the edges of the micro-magnets, where the magnetic force acting on the nanoparticles is the highest. At the final zones, large micro-magnets and the slow flow create large capture zones for capturing cells with low levels of surface marker expression. In order to determine the size of a capture zone for the cells having high, medium, low levels of magnetic loading, the radius (measured from the center of the 'X'-structure) of the capture zone was measured at the height of 10 μm along the length of the chip (Figure S1.B). It is worth noting that the radius of capture zone is restricted to the maximum of 325 μm based on the distance between adjacent X-structures.

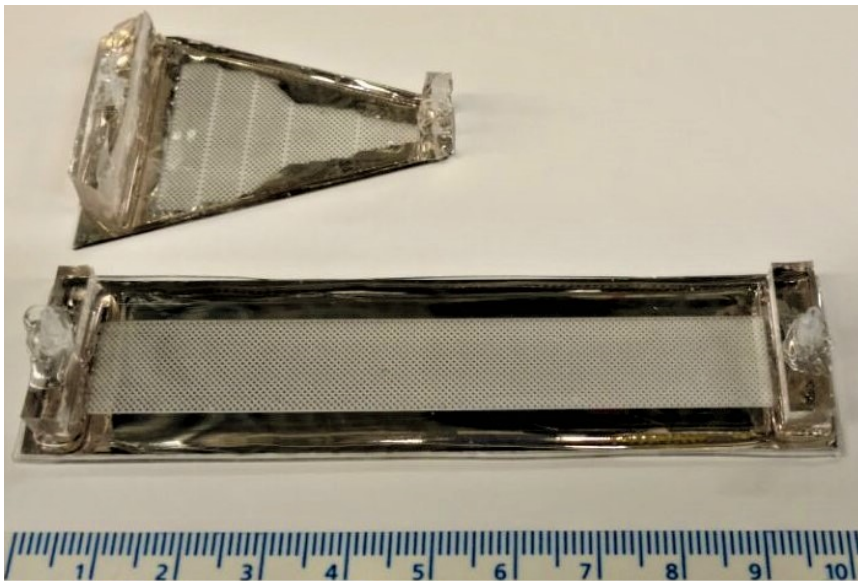

Figure S1. Comparing designs of the next generation of MagRC and original MagRC. Length of the channel is decreased by half in the next generation of MagRC which results in a reduction in fabrication time and cost (Related to Figure 1).

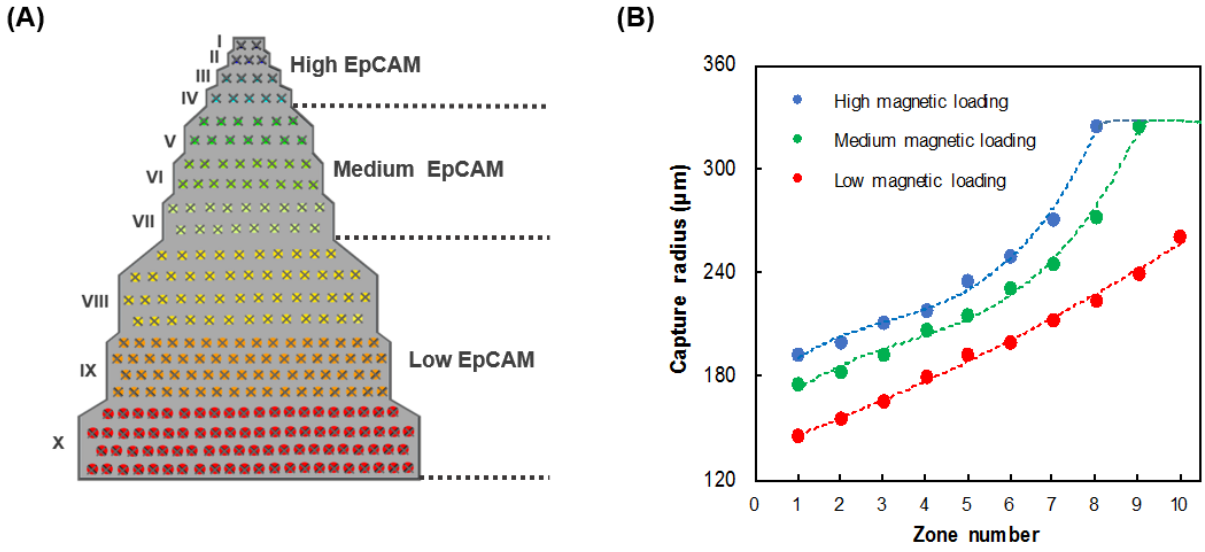

Figure S2. The new generation of MagRC design and modeling. (A) Schematic of the new generation of MagRC. (B) Calculation of the capture zone radius versus zone number in the new generation of MagRC. (Related to Figure 1).

Performance assessment of the device using cultured cells

To validate the performance of the device, cultured cell lines with known EpCAM expression levels were introduced to the device. Three cell lines were used to validate the sorting capacity of the device, including VCaP, SKBR3 and MDA-MB-231 with high, moderate and low expression of EpCAM, respectively. VCaP is an epithelial prostate cancer cell line (Wu et al., 2013), SKBR3 is a breast adenocarcinoma cell line and MDA-MB-231 is a breast cancer cell line with mesenchymal phenotype (Green et al., 2017). 100 cells were spiked in PBS buffer and incubated with EpCAM magnetic nanobeads. After 30 minutes, magnetized cells were loaded into the microfluidic channel at 400 µl/h using a syringe pump. Cells were captured in the device under the influence of an external magnetic field applied via upper and lower arrays of magnets. A nuclear marker was used to stain the captured cells. Later, cells that were trapped in each zone were detected and enumerated. The distribution of CTCs in the device was then plotted against the number of zones (Figure S3). Reproducibility of the results was confirmed by repeating each experiment at least three times. High capture efficiencies were achieved for all three cell lines (Figure 1.C). Remarkably, even MDA-MB-231 cells with very low EpCAM expression were captured with high efficiency.

Based on the capture principles of the device, we expect to find high EpCAM-expressing cells in early zones where the nickel micromagnets are smaller and channel is narrower, while cells with lower expression

would be captured in later zones with bigger nickel micromagnets and larger capture areas. Our experimental data obtained using cultured cells were in line with these principles. VCaP cells with the highest level of EpCAM expression were mainly captured in early zones of the device. In contrast, MDA-MB-231 cells, with lowest expression levels were captured in the zones near the outlet of the chip, and moderately expressing SKBR3 cells, were distributed in middle zones. The profiling capability of the device was confirmed by comparing the profiles collected from zone-based enumeration of captured cells with flow cytometric profiles of EpCAM expression in the cell lines (inset to Figure 1.B). The significant advantage of this technique over flow cytometry is that it is amenable to samples with low numbers of the target cells while flow cytometry needs at least 104 cells to provide reliable results. Also, cancer cells in unprocessed blood samples cannot be analyzed by flow cytometry, which can be easily analyzed by our device (will be demonstrated in the next section). Statistical analysis demonstrates that these profiles are significantly distinct from each other. The p-values (<0.0001) obtained from t-test analysis reports on the high levels of resolution in this device. Finally, the sensitivity of the device was challenged by processing samples with very low numbers of cells, as low as 10 cells (Figure 1.D). The number of recovered cells are very close to the actual number of cells measured by hemocytometer prior to loading into the device.

Although we are mainly focusing on EpCAM profiles of different cell populations here, this technique is highly versatile and is not solely limited to EpCAM profiling. Other surface markers such as anti-N-Cadherin and anti-HER2 can be conjugated to magnetic nanoparticles and used as the capture and profiling agent (Poudineh et al., 2016).

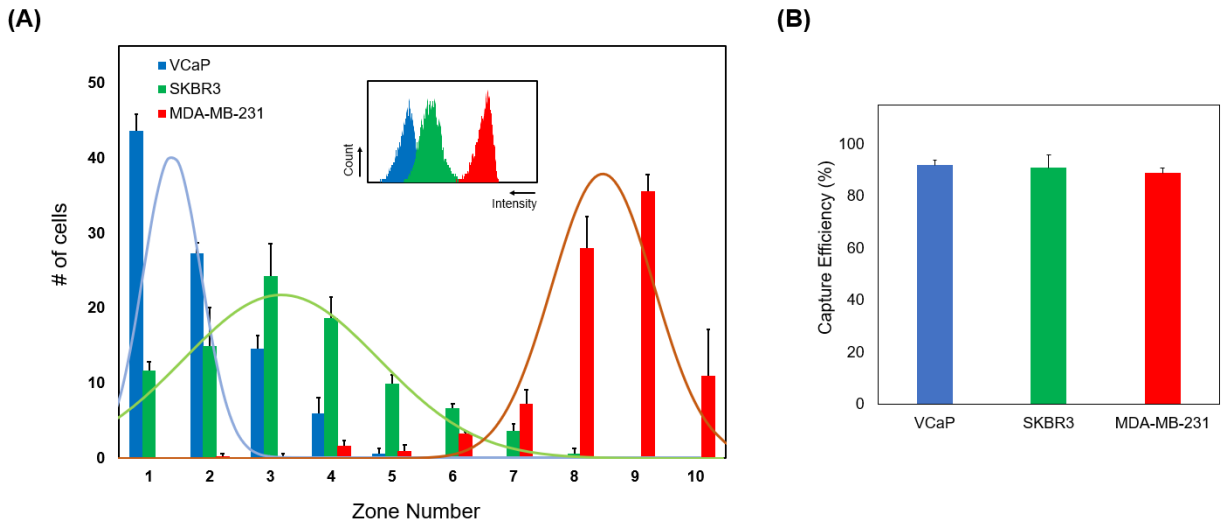

Figure S3. Performance assessment of the new MagRC microfluidic platform. (A) EpCAM expression profiles in three cell lines with different phenotypes: VCaP, SKBR3 and MDA-MB-231. Each profile represents the data collected from at least three trials. Cells were suspended in PBS buffer and stained with DAPI (nuclear stain). Insets,

phenotypic profiles obtained from 100-zone MagRC device and EpCAM expression levels measured by flow cytometry; (B) Capture efficiencies of VCaP, SKBR3 and MDA-MB-231cells; (C) Sensitivity analysis of the device: the microfluidic device was challenged with low number of cells. Error bars represent data from three trials. (Related to Figure 2).

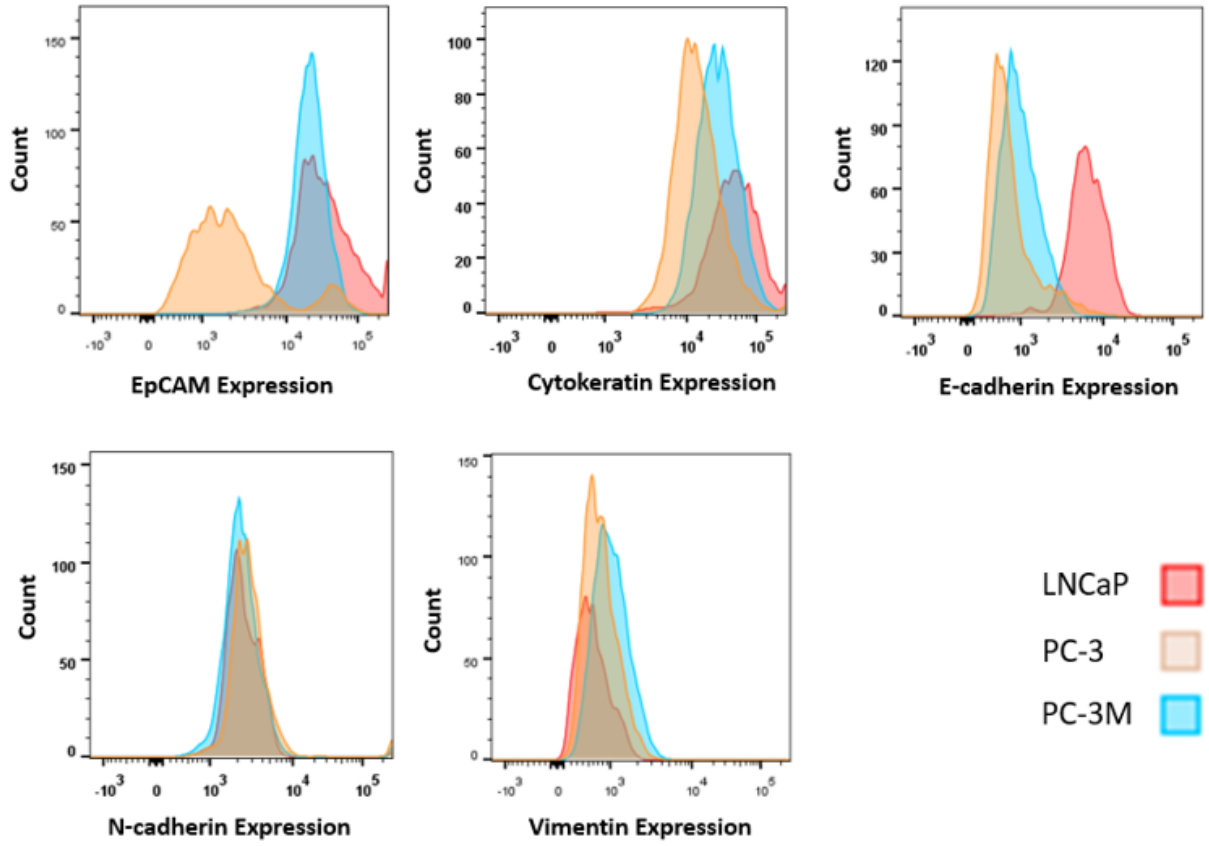

Figure S4. Characterization of prostate cancer cell lines based on their protein expression. Expression levels of epithelial and mesenchymal markers are measured in LNCaP, PC-3 and PC-3M cells. The results display differences in EMT phenotype in these cells (Related to Figure 2).

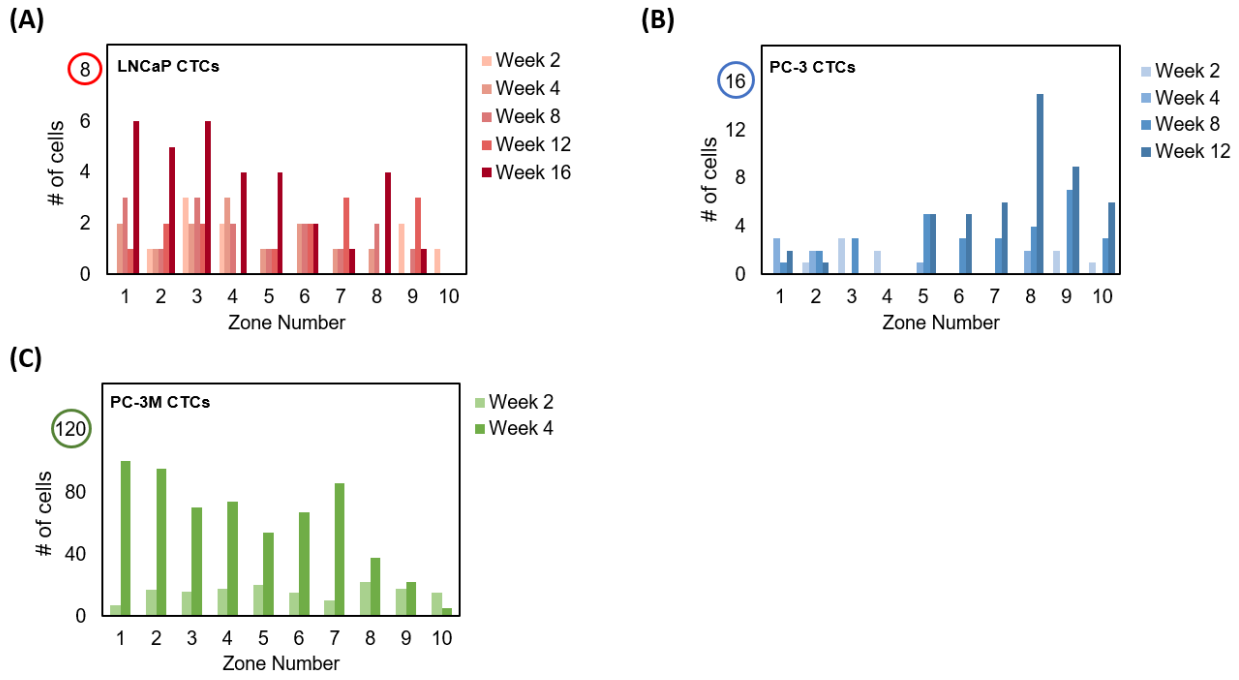

Figure S5. CTC analysis in mouse xenografts. EpCAM-based CTC distributions in (A) LNCaP, (B) PC-3 and (C) PC-3M xenograft mouse models. In general, CTCs in LNCaP xenografts are mostly localized in early zones. The p-value obtained from t-test analysis indicates that there is no significant difference between CTC phenotypic profiles from week 2 to week 16 ($p=0.3696$). In PC-3 xenografts, however, a significant phenotypic shift is detected during disease progression from week 2 to week 12 ($p<0.0001$) (Related to Figure 3).

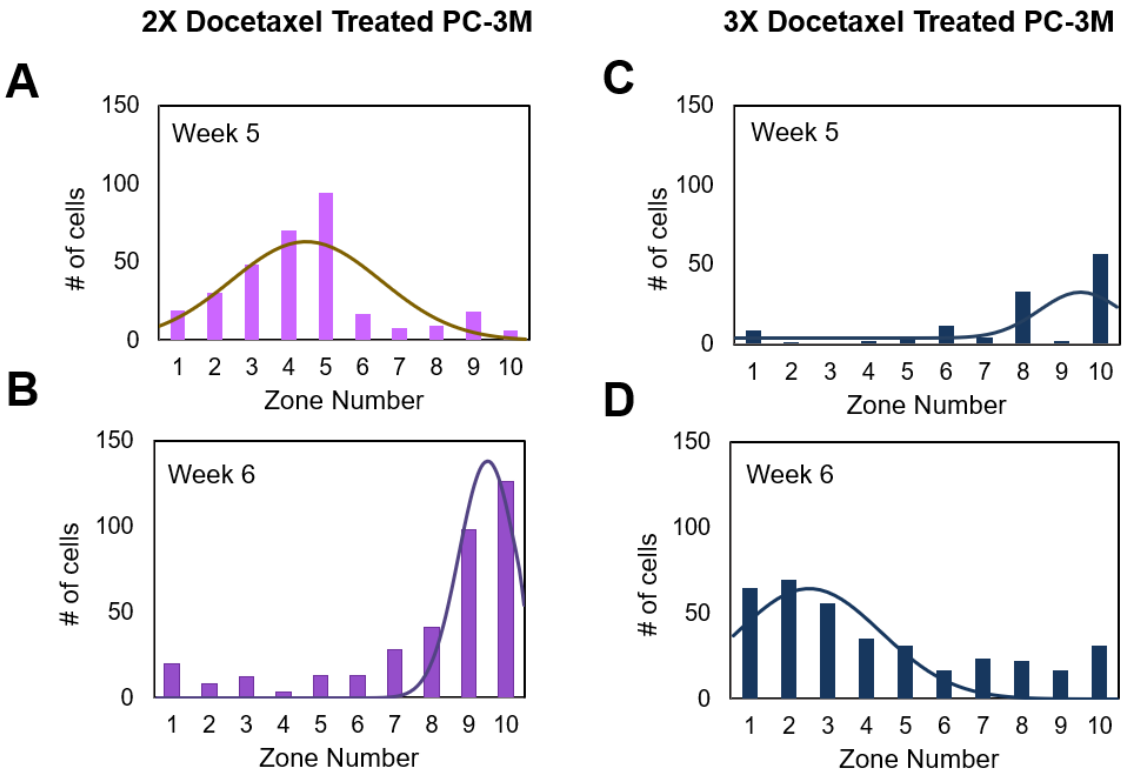

Figure S6. Effects of docetaxel treatment on PC-3M mouse xenografts and CTCs. (A) CTC profile in PC-3M mice treated with 2 doses of docetaxel 5 weeks post-injection. (B) CTC profile in PC-3M mice treated with 2 doses of docetaxel 6 weeks post-injection. (C) CTC profile in PC-3M mice treated with 3 doses of docetaxel 5 weeks post-injection. (D) CTC profile in PC-3M mice treated with 3 doses of docetaxel 6 weeks post-injection.